





**Nonlinear optical properties and Kerr nonlinearity of Rydberg excitons in Cu<sub>2</sub>O quantum wells**David Ziemkiewicz <sup>\*</sup>, Gerard Czajkowski , Karol Karpiński , and Sylwia Zielińska-Raczyńska *Institute of Mathematics and Physics, Technical University of Bydgoszcz, Al. Prof. S. Kaliskiego 7, 85-789 Bydgoszcz, Poland*

(Received 14 June 2022; revised 25 July 2022; accepted 24 August 2022; published 31 August 2022)

The quantum confinement of Rydberg excitons (REs) in quantum structures opens the way towards considering nonlinear interactions in such systems. We present a theoretical calculation of optical functions in the case of a nonlinear coupling between REs in a quantum well with an electromagnetic wave. Using the real density matrix approach (RDMA), the analytical expressions for a linear and nonlinear absorption are derived and numerical calculations for Cu<sub>2</sub>O quantum wells are performed. The results indicate the conditions in which quantum well confinement states can be observed in linear and nonlinear optical spectra. The Kerr nonlinearity and self-phase modulation in such a system are studied. The effect of the Rydberg blockade and the associated optical bleaching are also discussed and confronted with available experimental data.

DOI: [10.1103/PhysRevB.106.085431](https://doi.org/10.1103/PhysRevB.106.085431)**I. INTRODUCTION**

Rydberg physics in semiconductors started in 2014 with an observation of highly excited excitonic states with principal quantum numbers as high as  $n = 25$  in cuprous oxide, the material of a very large exciton binding energy [1]. This experiment revealed a plethora of Rydberg excitons' unusual properties such as extraordinary large dimensions up to  $1 \mu\text{m}$ , long lifetimes on the order of a nanosecond, vulnerability to interactions with external fields, and restrictions of their coupling arising from the Rydberg blockade, which precludes a simultaneous excitation of two Rydberg excitons that are separated by less than a blockade radius  $r_b$ . Many papers have been devoted to studies of spectroscopic characteristics of REs in natural and synthetic bulk systems of Cu<sub>2</sub>O [2–4] (see more references therein). Simultaneously, the explorations of RE in the field of quantum optics have begun by demonstration of a generation and control of strong excitonic interactions with the help of a two-color pump-probe technique [5], Rydberg exciton-assisted coupling between microwave and optical fields [6], and the experimental verification of the strong coupling of REs to cavity photons [7]. Moreover, some efforts have been made to investigate nonlinear interactions of REs with electromagnetic fields [8,9]. The recent one-photon experiment has shown a giant nonlinear optical index in a bulk Cu<sub>2</sub>O crystal, caused by sharp Rydberg resonances and revealed a Kerr phase shift much larger than in typical nonlinear crystals [10]. Interesting, giant microscopic dimensions of Rydberg excitons together with an intrinsic Rydberg blockade effect in cuprous oxide cause enhanced nonlinearities at much smaller densities compared with other semiconductors [1,11].

Those results indicate that Rydberg excitons are a unique platform for obtaining strong interactions in solid systems and allow one to hope for a realization, in a close future, of solid state masers [12,13] and few-photon devices. The first

step to achieve a scalable solid-state platform characterized by controlled interactions between Rydberg excitons and photons is to realize such technologically demanding miniaturized systems, consisting of an investigation of REs' properties in strongly confined systems such as quantum dots, wires, or wells [14–17]. The experiment, which has verified a change of oscillator strength due to quantum confinement of REs in a nanoscale system [17], is an important step towards exploiting their large nonlinearities for quantum applications. The recent progress in fabricating synthetic cuprous oxide elements has shown an enormous progress of their quality manifested by observations of high excitonic states [4,18,19] and now the natural direction of subsequent explorations seems to be the study of a nonlinear interaction between confined REs and light. A great challenge in quantum optics is an accomplishment of the gigantic Kerr nonlinearities in solid-state low-dimensional media. This phenomenon was realized in semiconductor quantum wells mostly under the conditions of the electromagnetically induced transparency [20–22] or in ultrathin gold films [23]. In our paper we propose a realization of the Kerr nonlinearity in the Cu<sub>2</sub>O quantum well with REs, taking advantage of the fact that confinement effects result in a significant optical Kerr susceptibility.

The theoretical tool which we use to calculate the optical functions for nonlinear interaction of electromagnetic radiation with Rydberg excitons in a quantum well is a mesoscopic method, called real density matrix approach [24–26]. This method can be understood as a generalization of the well-known Maxwell-Bloch theory of atoms interacting with resonant radiation. In the following we treat electromagnetic processes in a two-band model where the semiconductor is considered as a collection of two level “atoms” with level spacing  $\hbar\omega_g$  and with the additional possibility of intraband motion, given by the band dispersion. The basic equations of RDMA, the so-called constitutive equations, describing the dynamics of the two-band system, provide a rather general framework for the simultaneous treatment of interband and intraband processes in a semiconductor, including their mutual

<sup>\*</sup>david.ziemkiewicz@utp.edu.pl

interaction. The RDMA has been applied to the optical excitation spectra of semiconductor bulk crystals, semiconductor superlattices, some low dimensional structures, and recently in the theory of optical properties of Rydberg excitons in nanostructures (for example, see [27] and references therein). The advantage of RDMA with respect to the quantum-mechanical standard calculation of the optical properties is that all coherence effects are automatically included, since we consider the probability amplitude rather than its absolute value. The detailed description of RDMA as well as a presentation of the iteration procedure, which allows one to obtain a nonlinear susceptibility for Rydberg excitons confined in a quantum well, is presented in Secs. II and III. The effect of the Rydberg blockade is also included in our treatment and is considered in Sec. IV. Phase-sensitive Kerr nonlinearity appearing in the discussed system is examined in Sec. V. Section VI contains the presentation of numerical results and their discussion, while the summary and conclusions of our paper are presented in Sec. VII.

## II. REAL DENSITY MATRIX APPROACH

### A. Basic equations

Our discussion follows the scheme of Refs. [8,10] adapted for the case of a quantum well. In the RDMA approach that nonlinear response will be described by a set of three coupled constitutive equations: for the coherent amplitude  $Y(\mathbf{r}_1, \mathbf{r}_2)$  representing the exciton density, for the density matrix  $C(\mathbf{r}_1, \mathbf{r}_2)$  for electrons (assuming a nondegenerate conduction band), and for the density matrix for the holes  $D(\mathbf{r}_1, \mathbf{r}_2)$  in the valence band. Denoting  $Y(\mathbf{r}_1, \mathbf{r}_2) = Y_{12}$ , the constitutive equations take the following form [16]:

(i) for the coherent amplitude

$$i\hbar\partial_t Y_{12} - H_{\text{QW}}Y_{12} = -\mathbf{M}\mathbf{E}(\mathbf{R}_{12}) + \mathbf{E}_1\mathbf{M}_0C_{12} + \mathbf{E}_2\mathbf{M}_0D_{12} + i\hbar\left(\frac{\partial Y_{12}}{\partial t}\right)_{\text{irrev}}, \quad (1)$$

(ii) for the conduction band

$$i\hbar\partial_t C_{12} + H_{ee}C_{12} = \mathbf{M}_0(\mathbf{E}_1Y_{12} - \mathbf{E}_2Y_{21}^*) + i\hbar\left(\frac{\partial C_{12}}{\partial t}\right)_{\text{irrev}}, \quad (2)$$

(iii) for the valence band

$$i\hbar\partial_t D_{21} - H_{hh}D_{21} = \mathbf{M}_0(\mathbf{E}_2Y_{12} - \mathbf{E}_1Y_{21}^*) + i\hbar\left(\frac{\partial D_{21}}{\partial t}\right)_{\text{irrev}}, \quad (3)$$

where the operator  $H_{\text{QW}}$  is the quantum well Hamiltonian, which includes the terms  $V_e, V_h$  related to the electron and hole confinement and the mutual Coulomb interaction  $V_{eh}$ ,

$$H_{\text{QW}} = E_g - \frac{\hbar^2}{2m_e}\partial_{z_e}^2 - \frac{\hbar^2}{2m_h}\partial_{z_h}^2 - \frac{\hbar^2}{2M_{\text{tot}}}\nabla_{R_{\parallel}}^2 - \frac{\hbar^2}{2\mu}\nabla_{\rho}^2 + V_e(z_e) + V_h(z_h) + V_{eh}, \quad (4)$$

with the separation of the center-of-mass coordinate  $\mathbf{R}_{\parallel}$  from the relative coordinate  $\rho$  on the plane  $(x, y)$ , e.g.,  $\rho = (r_1 -$

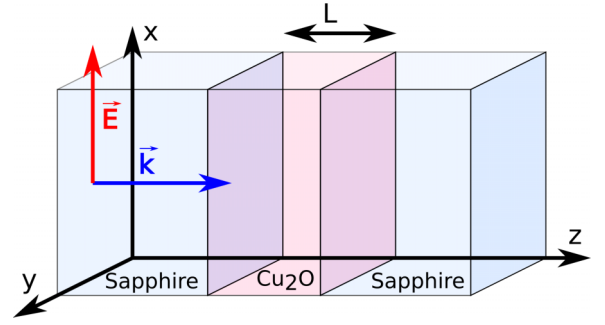


FIG. 1. Schematic representation of the considered QW system.

$r_2)_{\parallel}$  and

$$H_{ee} = -\frac{\hbar^2}{2m_e}(\nabla_1^2 - \nabla_2^2), \quad (5)$$

$$H_{hh} = -\frac{\hbar^2}{2m_h}(\nabla_1^2 - \nabla_2^2),$$

and  $\mathbf{E}_1 = \mathbf{E}(\mathbf{r}_1)$ ,  $\mathbf{E}_2 = \mathbf{E}(\mathbf{r}_2)$ . In the case of a quantum well with thickness that is significantly smaller than the light wavelength, one can assume uniform field  $\mathbf{E}_1 = \mathbf{E}_2 = \mathbf{E}$ . The center of the mass coordinate is

$$\mathbf{R} = \mathbf{R}_{12} = \frac{m_h\mathbf{r}_1 + m_e\mathbf{r}_2}{m_h + m_e}. \quad (6)$$

In the above formulas  $m_e, m_h$  are the electron and the hole effective masses (the effective mass tensors in general),  $M_{\text{tot}}$  is the total exciton mass, and  $\mu$  the reduced mass of electron-hole pair. The smeared-out transition dipole density  $\mathbf{M}(\mathbf{r})$  is related to the bilocality of the amplitude  $Y_{12}$  and describes the quantum coherence between the macroscopic electromagnetic field and the interband transitions (see, for example, Refs. [24,25]); the detailed derivation of  $\mathbf{M}(\mathbf{r})$  is described in Ref. [28]. We consider the response of the quantum well with surfaces located at  $z = \pm L/2$ , to a normally incident electromagnetic wave, linearly polarized in the  $x$  direction. The schematic of the system is shown in Fig. 1. We assume that the carrier motion in the  $z$  direction is governed by the no-escape boundary conditions. With this assumptions, the QW Hamiltonian has the form

$$H_{\text{QW}} = E_g + \frac{p_{z_e}^2}{2m_e} + \frac{p_{z_h}^2}{2m_h} + V(z_e) + V(z_h) + H_{\text{Coul}}^{(2D)}(\rho), \quad (7)$$

where

$$V(z_{e,h}) = 0 \quad \text{for } 0 \leq z \leq L, \quad (8)$$

$$V(z_{e,h}) = \infty \quad \text{for } z < 0, \quad z > L,$$

$H_{\text{Coul}}^{(2D)}$  is the two-dimensional Coulomb Hamiltonian

$$H_{\text{Coul}}^{(2D)}(\rho) = \frac{\mathbf{p}_{\parallel}^2}{2\mu_{\parallel}} - \frac{e^2}{4\pi\epsilon_0\epsilon_b\rho}. \quad (9)$$

We consider here the strong confinement regime, where the confinement energy exceeds the Coulomb energy. The resulting coherent amplitude  $Y_{12}$  determines the excitonic part of the

polarization of the medium

$$\begin{aligned} \mathbf{P}(\mathbf{R}, t) &= 2 \int d^3r \mathbf{M}^*(\mathbf{r}) \text{Re} Y_{12}(\mathbf{R}, \mathbf{r}, t) \\ &= \int d^3r \mathbf{M}^*(\mathbf{r}) [Y_{12}(\mathbf{R}, \mathbf{r}, t) + \text{c.c.}], \end{aligned} \quad (10)$$

where  $\mathbf{r} = \mathbf{r}_1 - \mathbf{r}_2$  is the electron-hole relative coordinate. The linear optical functions are obtained by solving the inter-band equation (1) together with the corresponding Maxwell equation, where the polarization (10) acts as a source. Using the entire set of constitutive equations (1)–(3) one can compute the nonlinear optical functions. While a general solution of this problem seems to be inaccessible, in some specific situations such a solution can be found, i.e., if one assumes that the matrices  $Y$ ,  $C$ , and  $D$  can be expanded in powers of the electric field  $\mathbf{E}$ , an iteration scheme can be used.

The relevant expansion of the polarization in powers of the field has the form

$$\begin{aligned} P(\mathbf{k}, \omega) &= \epsilon_0 E(\mathbf{k}, \omega) [\chi^{(1)} + \chi^{(3)}(\omega, -\omega, \omega) \\ &\quad \times |E(\mathbf{k}, \omega)|^2 + \dots], \end{aligned} \quad (11)$$

where  $\chi^{(1)}$  and  $\chi^{(3)}$  are the linear and the nonlinear parts of the susceptibility. Although the above equations apparently resemble those describing the nonlinear case of the bulk crystal with Rydberg excitons [8], we present a full theoretical approach for the sake of completeness and it should be stressed that taking into account the confinement interaction significantly changes the results. It should be stressed that in our two-dimensional exciton model, the electron and the hole move in the  $xy$  plane upon the action of the two-dimensional Coulomb potential, and are confined in the  $z$  direction. Thus the confinement and the exciton states are separated and the confinement does not depend on the main quantum number. Such a simplification is justified by the fact that the exciton energies for higher exciton states, in the two-dimensional simplification, are practically equal to the corresponding three-dimensional exciton states. A further discussion of the transition between two and three dimensions, in the framework of the RDMA, is given in [15].

### B. Iteration

We calculate the QW optical functions iteratively from the constitutive equations (1)–(3). The first step in the iteration consists of solving Eq. (1) (skipping the second and third terms on its right-hand side) which we take in the form

$$i\hbar \partial_t Y_{12}^{(1)} - H_{\text{QW}} Y_{12}^{(1)} = -\mathbf{M}\mathbf{E} + i\hbar \left( \frac{\partial Y_{12}^{(1)}}{\partial t} \right)_{\text{irrev}}. \quad (12)$$

It should be mentioned that we use the long-wave approximation, which allows us to neglect the spatial distribution of the electromagnetic wave inside the quantum well.

For the irreversible part, assuming a relaxation time approximation, one gets

$$\left( \frac{\partial Y_{12}^{(1)}}{\partial t} \right)_{\text{irrev}} = -\frac{1}{T_2} Y_{12} = \frac{-\Gamma}{\hbar} Y_{12}. \quad (13)$$

with  $\Gamma = \hbar/T_2$  being a dissipation constant. Considering nonlinear effects, the nonresonant parts of the coherent amplitude

$Y$  have to be taken into account; so for the electric field  $\mathbf{E}$  in the medium of the form

$$\mathbf{E} = \mathbf{E}(\mathbf{R}, t) + \mathbf{E}^*(\mathbf{R}, t) = \mathbf{E}_0 e^{i(\mathbf{k}\mathbf{R} - \omega t)} + \mathbf{E}_0 e^{-i(\mathbf{k}\mathbf{R} - \omega t)}, \quad (14)$$

Eq. (12) generates two equations: one for an amplitude  $Y_{12+}^{(1)} \propto \exp(-i\omega t)$ , and the second for the nonresonant part  $Y_{12-}^{(1)} \propto \exp(i\omega t)$ ,

$$\begin{aligned} i\hbar \left( i\omega + \frac{1}{T_2} \right) Y_{12+}^{(1)} - H_{eh} Y_{12+}^{(1)} &= -\mathbf{M}\mathbf{E}^*(\mathbf{R}, t), \\ i\hbar \left( -i\omega + \frac{1}{T_2} \right) Y_{12-}^{(1)} - H_{\text{QW}} Y_{12-}^{(1)} &= -\mathbf{M}\mathbf{E}(\mathbf{R}, t). \end{aligned} \quad (15)$$

In what follows we consider only one component of both  $\mathbf{E}$  and  $\mathbf{M}$ . Similarly, as in Ref. [8], we look for the solution in terms of eigenfunctions of the Hamiltonian  $H_{\text{QW}}$ , which now contains the confinement terms, so these eigenfunctions have the following form:

$$\Psi_{jmN_eN_h}(r, \phi, z_e, z_h) = \psi_{jm}(r, \phi) \psi_{L,N_e}^{(1D)}(z_e) \psi_{L,N_h}^{(1D)}(z_h), \quad (16)$$

where  $\mathbf{r} = (r, \phi)$  is the two-dimensional space vector,  $\psi_{jm}$  are the normalized eigenfunctions of the two-dimensional Coulomb Hamiltonian,

$$\begin{aligned} \psi_{jm}(r, \phi) &= R_{jm}(r) \frac{e^{im\phi}}{\sqrt{2\pi}}, \\ R_{jm} &= C_{jm} \left( 4\kappa \frac{r}{a^*} \right)^m e^{-2\kappa_{jm} r/a^*} \\ &\quad \times M \left( -j, 2|m| + 1, 4\kappa_{jm} \frac{r}{a^*} \right), \\ \kappa_{jm} &= \frac{1}{1 + 2(j + |m|)}, \\ C_{jm} &= \frac{1}{a^*} 4\kappa_{jm}^{3/2} \frac{1}{(2m)!} \frac{[(j + 2m)!]^{1/2}}{[j!]^{1/2}}, \end{aligned} \quad (17)$$

with the Kummer function [29]  $M(a, b, z)$  (the confluent hypergeometric function), and  $\psi_{\alpha,N}^{(1D)}(z)$  ( $N = 0, 1, \dots$ ) are the quantum oscillator eigenfunctions of the Hamiltonian (8)

$$\begin{aligned} \psi_{L,N_e}^{(1D)}(z_e) &= \sqrt{\frac{2}{L}} \cos \left[ (2N_e - 1)\pi \frac{z_e}{L} \right], \\ \psi_{L,N_h}^{(1D)}(z_h) &= \sqrt{\frac{2}{L}} \cos \left[ (2N_h - 1)\pi \frac{z_h}{L} \right]. \end{aligned}$$

The role of the amplitude  $Y_{12}^{(1)}$  obtained in such a way is twofold. First, substituting into Eq. (10) gives the linear excitonic polarization  $P^{(1)}$  and from the relation  $P^{(1)} = \epsilon_0 \chi^{(1)} E$  we can calculate the mean effective linear susceptibility, which is given by the following expression:

$$\chi^{(1)}(\omega) = \chi_0^{(1)} \left( \frac{a^*}{L} \right) \sum_0^{N_{\max}} \sum_{j=0}^J \frac{f_j^{(2D)} E_{TjN}}{E_{TjN}^2 - (\hbar\omega + i\Gamma_j)^2}, \quad (18)$$

where the summation is over the confinement state number  $N$  and excitonic state number  $j$ , where  $j = 0$  is the lowest

excitonic state. The oscillator strengths  $f_j^{(2D)}$  are given by

$$f_j^{(2D)} = 48 \frac{(j+1)(j+2)}{(j+3/2)^5} \frac{1}{(1+2\kappa_j\rho_0)^8} \times \left[ F\left(-j, 4; 3; \frac{4\kappa_j\rho_0}{1+2\kappa_j\rho_0}\right) \right]^2, \quad (19)$$

$$\kappa_j = \frac{1}{2j+3},$$

and the energy terms, including exciton binding energy  $E_j$  and quantum well contribution  $W_N$  are as follows:

$$E_{TjN} = E_g + W_N + E_j, \quad (20)$$

$$W_N = \left(\frac{N\pi a^*}{L}\right)^2 R^*, \quad N = 1, 2, \dots,$$

$$E_j = -\frac{1}{(j+1-\delta)^2} R^*, \quad j = 0, 1, 2, \dots$$

$a^*$  is the effective exciton Bohr radius,  $R^*$  is the exciton Rydberg energy,  $\rho_0 = r_0/a^*$  defines the coherence radius, and  $F(a, b; c, z)$  is the hypergeometric series [29]. The coherence radius  $r_0 = [(2\mu/\hbar^2)E_g]^{-1/2}$ ,  $E_g$  is the fundamental gap, and  $\mu$  is reduced effective mass of the electron-hole pair. The  $\delta = 0.2$  is the so-called quantum defect [1]; it should be mentioned that while the most common value of  $\delta$  is used here, smaller ones provide a better fit to many experimental results, especially at elevated temperatures [30]. The constant factor  $\chi_0^{(1)}$  has the form

$$\chi_0^{(1)} = \epsilon_b e^{-4\rho_0} \Delta_{LT}. \quad (21)$$

For simplicity we can use only one confinement state number by considering only the largest contribution from  $N_e = N_h = N$ . Due to the long-wave approximation, the validity of our considerations is limited regarding the quantum well width  $L$ , which in turn entails the restriction of the highest observable confinement states  $N_{\max}$ . Specifically, in the case of a thin quantum well, the considerable confinement energy  $W_N$  means that for higher  $N$  and  $j$ , the total energy  $E_{TjN}$  approaches the band gap, where higher absorption precludes the observation of confinement states. Regardless of the possibility of observing the confinement states on the absorbing background of band gap, another upper limit on  $N_{\max} \sim 10$  is provided if we assume that confinement energy cannot exceed exciton binding energy.

### III. ITERATION PROCEDURE: SECOND STEP

Again, in order to present the detailed derivation of nonlinear susceptibility for a quantum well with Rydberg excitons, we recall the procedure in general similar to that presented in [8], but considering here the low dimensional systems significantly changes the final results. Let us first consider a wave linearly polarized in the  $x$  direction. Then  $Y_{\pm}^{(1)}$  (15) are inserted into the source terms of the conduction-band and valence-band equations (2) and (3). Solving for stationary solutions and making the long-wave approximation, we obtain

for both source terms

$$J_C = M_0\rho_0(E_1Y_{12}^{(1)} - E_2Y_{21}^{(1)*}) = \frac{2iM_0\rho_0E_0^2}{\hbar} [\text{Im}g(-\omega, \mathbf{r}) + \text{Im}g(\omega, \mathbf{r})] = J_V, \quad (22)$$

where

$$g(\pm\omega, \mathbf{r}) = \sum_j \frac{c_{jmN_eN_h} \Phi_{jmN_eN_h}(\mathbf{r})}{\Omega_{jmN_eN_h} \mp \omega - i/T_{2jm}}. \quad (23)$$

If irreversible terms are well defined, Eqs. (3) can be solved and their solutions are then used in the saturating terms on the right-hand side (r.h.s.) of Eq. (1). Again, as in the previous section, we will use a relaxation time approximation and the equations for the matrices  $C$  and  $D$  are as follows:

$$\left(\frac{\partial C}{\partial t}\right)_{\text{irrev}} = -\frac{1}{\tau} [C(\mathbf{X}, \mathbf{r}, t) - f_{0e}(\mathbf{r})C(\mathbf{X}, \mathbf{r} = \mathbf{r}_0, t)] - \frac{C(r_0)}{T_1},$$

$$\left(\frac{\partial D}{\partial t}\right)_{\text{irrev}} = -\frac{1}{\tau} [D(\mathbf{X}, \mathbf{r}, t) - f_{0h}(\mathbf{r})D(\mathbf{X}, \mathbf{r} = \mathbf{r}_0, t)] - \frac{D(r_0)}{T_1}, \quad (24)$$

where

$$\mathbf{X} = \frac{1}{2}(\mathbf{r}_e + \mathbf{r}_h), \quad (25)$$

and  $f_{0e}$ ,  $f_{0h}$  are normalized Boltzmann distributions for electrons and holes, respectively. The relaxation parameter  $T_1$  is due to interband recombination [31] and  $\tau = 1/\Gamma_j \ll T_1$  is the lifetime corresponding to radiative recombination. The functions  $C$ ,  $D$  must have the same  $p$  symmetry as the amplitudes  $Y$ . Thus we use the transport current density

$$\mathbf{j}_n(\mathbf{r}) = \frac{i\hbar}{2m_e} (\nabla_1 - \nabla_2)|_{\mathbf{r}_1=\mathbf{r}_2=\mathbf{r}}, \quad (26)$$

and take the  $x$  component, which leads to the following expression for the modified distribution for electrons:

$$\tilde{f}_{0e}(\mathbf{r}) = \int d^3q q_x f_{0e}(\mathbf{q}) e^{-i\mathbf{q}\mathbf{r}}, \quad (27)$$

with

$$f_{0e}(\mathbf{q}) = \sqrt{2\pi} \left(\frac{\hbar^2}{2\pi k_B \mathcal{T}}\right)^2 \exp\left(-\frac{\hbar^2 q^2}{2m_e k_B \mathcal{T}}\right), \quad (28)$$

where  $\mathcal{T}$  is the temperature and  $k_B$  is the Boltzmann constant. The integral (27) can be evaluated analytically yielding

$$\begin{aligned} \tilde{f}_{0e}(\mathbf{r}) &= \tilde{f}_{0e}(\rho, z_e, z_h, \phi) \\ &= \sqrt{\frac{\pi}{2}} \frac{r}{\lambda_{\text{the}}} [\Phi_1(\phi) + \Phi_{-1}(\phi)] \\ &\quad \times \exp\left(-\frac{r^2 + (z_e - z_h)^2 m_e k_B \mathcal{T}}{2\hbar^2}\right) \\ &= \tilde{f}_{0e}^{\perp}(z_e, z_h) \tilde{f}_{0e}^{\parallel}(r, \phi), \\ \tilde{f}_{0e}^{\perp}(z_e, z_h) &= \exp\left(-\frac{(z_e - z_h)^2 m_e k_B \mathcal{T}}{2\hbar^2}\right), \end{aligned}$$

$$\begin{aligned} \tilde{f}_{0e}^{\parallel}(r, \phi) &= \sqrt{\frac{\pi}{2}} \frac{r}{\lambda_{\text{the}}} \exp\left(-\frac{r^2 m_e k_B \mathcal{T}}{\hbar^2}\right) \\ &\times [\Phi_1(\phi) + \Phi_{-1}(\phi)], \\ r &= \sqrt{x^2 + y^2}, \end{aligned} \quad (29)$$

where

$$\Phi_m(\phi) = \frac{e^{im\phi}}{\sqrt{2\pi}} \quad (30)$$

and

$$\lambda_{\text{the}} = \left(\frac{\hbar^2}{m_e k_B \mathcal{T}}\right)^{1/2} = \sqrt{\frac{2\mu}{m_e}} \sqrt{\frac{R^*}{k_B \mathcal{T}}} a^* \quad (31)$$

is the so-called thermal length (here for electrons). Similarly, for the hole equilibrium distribution we have

$$\begin{aligned} \tilde{f}_{0h}(\mathbf{r}) &= \tilde{f}_{0h}(\rho, z_e, z_h, \phi) \\ &= \sqrt{\frac{\pi}{2}} \frac{r}{\lambda_{\text{thh}}} [\Phi_1(\phi) + \Phi_{-1}(\phi)] \exp \\ &\times \left(-\frac{r^2 + (z_e - z_h)^2 m_h k_B \mathcal{T}}{\hbar^2}\right) \\ &= \tilde{f}_{0h}^{\perp}(z_e, z_h) \tilde{f}_{0h}^{\parallel}(r, \phi), \\ \tilde{f}_{0h}^{\perp}(z_e, z_h) &= \exp\left(-\frac{(z_e - z_h)^2 m_h k_B \mathcal{T}}{\hbar^2}\right), \\ \tilde{f}_{0h}^{\parallel}(r, \phi) &= \sqrt{\frac{\pi}{2}} \frac{r}{\lambda_{\text{thh}}} \exp\left(-\frac{r^2 m_h k_B \mathcal{T}}{\hbar^2}\right) \\ &\times [\Phi_1(\phi) + \Phi_{-1}(\phi)], \end{aligned} \quad (32)$$

with the hole thermal length

$$\lambda_{\text{thh}} = \left(\frac{\hbar^2}{m_h k_B \mathcal{T}}\right)^{1/2} = \sqrt{\frac{2\mu}{m_h}} \sqrt{\frac{R^*}{k_B \mathcal{T}}} a^*.$$

The matrices  $C$  and  $D$  are temperature dependent, so they also can be used as an additional contribution for interpretation of temperature variations of excitonic optical spectra. However, the temperature dependence of relaxation constants  $\Gamma_n$  remains a dominant mechanism influencing the spectra. Furthermore, we will assume that our medium is excited homogeneously in  $\mathbf{X}$  space. For  $p$  excitons the matrices  $C$  and  $D$  relax to their values at  $r = r_0$ . In  $\text{Cu}_2\text{O}$ , the dipole density

can be approximated by  $\mathbf{M}(\mathbf{r}) \propto \mathbf{r}\delta(r - r_0)$  [24], which leads to the following expressions for the matrices  $C$ ,  $D$ :

$$\begin{aligned} C(\mathbf{r}) &= -\frac{i}{\hbar} [\tau J_C(\mathbf{r}) - \tau J_C(r_0) + T_1 f_{0e}(\mathbf{r}) J_C(r_0)], \\ D(\mathbf{r}) &= -\frac{i}{\hbar} [\tau J_V(\mathbf{r}) - \tau J_V(r_0) + T_1 f_{0hH}(\mathbf{r}) J_V(r_0)]. \end{aligned} \quad (33)$$

With the above expression the equation for the third-order coherent amplitude  $Y_{12}^{(3)}$  takes the form

$$\begin{aligned} \hbar \left(\omega + \frac{i}{T_2}\right) Y_{12-}^{(3)} - H_{\text{QW}} Y_{12-}^{(3)} \\ = M_0 \rho_0 (E_1 C_{12} + E_2 D_{21}) = E(\mathbf{R}, t) \tilde{J}_-, \\ \hbar \left(-\omega + \frac{i}{T_2}\right) Y_{12+}^{(3)} - H_{\text{QW}} Y_{12+}^{(3)} \\ = M_0 \rho_0 (E_1^* C_{12} + E_2^* D_{21}) = E^*(\mathbf{R}, t) \tilde{J}_+. \end{aligned} \quad (34)$$

To define the source terms  $\tilde{J}_{\pm}$  we use the fact that for most semiconductors  $T_1 \gg \tau$ . Therefore we retain only the terms proportional to  $T_1$ , obtaining

$$\begin{aligned} \tilde{J}_- &= -\frac{i}{\hbar} T_1 M_0 \rho_0 \{J_C(r_0) \tilde{f}_{0e}(\mathbf{r}) + J_V(r_0) \tilde{f}_{0h}(\mathbf{r})\}, \\ \tilde{J}_+ &= -\frac{i}{\hbar} M_0 \rho_0 T_1 \{J_C(r_0) \tilde{f}_{0e}(\mathbf{r} + J_V(r_0) \tilde{f}_{0h}(\mathbf{r}))\}. \end{aligned} \quad (35)$$

From  $Y^{(3)}$  one finds the third-order polarization according to

$$\begin{aligned} P^{(3)}(\mathbf{R}) &= 2 \int d^3 r \text{Re} M(\mathbf{r}) Y^{(3)}(\mathbf{R}, \mathbf{r}) \\ &= \int d^3 r M(\mathbf{r}) (Y_{12-}^{(3)} + Y_{12+}^{(3*)}). \end{aligned} \quad (36)$$

As in the case of linear amplitudes  $Y^{(1)}$ , we expand the nonlinear amplitudes in terms of the eigenfunctions  $\Psi_{\ell m N_e N_h}(\mathbf{r})$ .

The next application of the amplitude  $Y_{12}^{(1)}$  is related to the iteration process. Inserting  $Y_{12}^{(1)}$  into the source terms on the r.h.s. of Eqs. (2) and (3) and using appropriate expressions for the irreversible terms, one obtains the matrices  $C^{(2)}$ ,  $D^{(2)}$ , where the superscript indicates the order with respect to the electric field strength  $E$ . Substituting the matrices into the saturating terms on the r.h.s. of Eq. (1) one obtains the equation for the nonlinear amplitude  $Y^{(3)}$  which, with respect to Eq. (10), defines the nonlinear susceptibility  $\chi^{(3)}$ . We obtain the following expression:

$$\chi^{(3)}(\omega) = -\left(\frac{a^*}{L}\right) \chi_0^{(3)} \sum_{j, \ell, N} \frac{\Gamma_j \mathcal{F}_{j\ell N} E_{T\ell N}}{[(E_{TjN} - \hbar\omega)^2 + \Gamma_j^2][E_{T\ell N}^2 - (E + i\Gamma_{\ell})^2]}, \quad (37)$$

where  $\ell = 0, 1, 2, \dots$ . The nonlinear oscillator strengths can be written as

$$\begin{aligned} \mathcal{F}_{j\ell N} &= \frac{M(-j, 3, 4\kappa_j \rho_0) M(-\ell, 3, 4\kappa_{\ell} \rho_0)}{(1 + 2\kappa_{\ell} \rho_0)^4 (1 + 2\kappa_j \rho_0)^4} F\left(-j, 4; 3; \frac{4\kappa_j \rho_0}{1 + 2\kappa_j \rho_0}\right) F\left(-\ell, 4; 3; \frac{4\kappa_{\ell} \rho_0}{1 + 2\kappa_{\ell} \rho_0}\right) \\ &\times \frac{(j+1)(j+2)}{(2j+3)^5} \frac{(\ell+1)(\ell+2)}{(2\ell+3)^2} \left[ \mathcal{A} \left(\frac{2}{2\ell+3}\right)^{\beta} V_{NN}^{(e)} + \mathcal{B} \left(\frac{2}{2\ell+3}\right)^{\gamma} V_{NN}^{(h)} \right], \\ \kappa_j &= \frac{1}{2j+3}, \quad \kappa_{\ell} = \frac{1}{2\ell+3}, \end{aligned} \quad (38)$$



where

$$\chi_0^{(3)} = \epsilon_0(\epsilon_b \Delta_{LT})^2 a^{*3} e^{-4\rho_0} \left( \frac{1}{\Gamma_1} \right) \quad (39)$$

and the derivation of constants  $\mathcal{A}$ ,  $\mathcal{B}$  is presented in Appendix A. The potentials  $V_{N_e N_h}$  are given by

$$\begin{aligned} V_{N_e N_h}^{(e)} &= \int_{-1}^1 dx \int_{-1}^1 dy \cos \left[ \frac{(2N_e - 1)\pi}{2} x \right] \cos \left[ \frac{(2N_h - 1)\pi}{2} y \right] \exp \left[ - \left( \frac{L^2}{8a^{*2} \tilde{\lambda}_{th,e}^2} \right) (x - y)^2 \right], \\ V_{N_e N_h}^{(h)} &= \int_{-1}^1 dx \int_{-1}^1 dy \cos \left[ \frac{(2N_e - 1)\pi}{2} x \right] \cos \left[ \frac{(2N_h - 1)\pi}{2} y \right] \exp \left[ - \left( \frac{L^2}{8a^{*2} \tilde{\lambda}_{th,h}^2} \right) (x - y)^2 \right], \end{aligned} \quad (40)$$

with the thermal lengths  $\tilde{\lambda}_{th,e,h}$  defined above in Eq. (31).

More detailed calculations of  $\chi^{(3)}$  are presented in Appendix B and the table of material parameters is included in Appendix C. The long-wave approximation we have used in the above calculations limits our results, which are appropriate for quantum wells thicknesses  $L$  significantly below  $1 \mu\text{m}$ .

#### IV. RYDBERG BLOCKADE

One of the important characteristics of the theoretical approach described above is the fact that it is derived under the assumption of a relatively low power level, when the medium is not saturated with excitons. Thus, the so-called Rydberg blockade [1] is not inherently present in the calculations and its effects have to be taken into account in a separate step. This has been done in Refs. [10,13] and the description outlined below is an extension of the approaches presented in the cited works.

For an exciton with principal quantum number  $(j + 1)$ , the blockade volume is given by [1]

$$V_B = 3 \times 10^{-7} (j + 1)^7 \mu\text{m}^3. \quad (41)$$

Similarly to the recent experiments [10], we assume that the laser beam illuminating the sample has a circular beam spot of area  $S$  of  $0.1 \text{ mm}^2$  and the sample length is  $L$ ; the volume, where the light can be absorbed and an exciton created is  $V = LS$ . Within this volume, a new exciton can be formed only when its location is outside of the blockade volume of existing excitons. Thus, assuming that the blockade volume is spherical, the upper limit of exciton density is the perfect sphere packing, where approximately 74% of the volume is occupied, e.g., for the number of excitons  $N_e$ ,  $N_e \frac{V_B}{V} \approx 0.74$ . However, the positions of the excitons formed within the laser beam are random and thus highly unlikely to form a perfect sphere packing. To estimate the practical upper limit of exciton density imposed by the Rydberg blockade, a Monte Carlo simulation has been performed; within given volume  $V$ , excitons with their associated blockade volumes are added at random positions, and the number of attempts to place an exciton in a free space (not occupied by blockade volume) is counted. Then, the probability of excitation (inverse of the number of attempts) is calculated. The results are shown in Fig. 2. One can see that the system is effectively saturated when the fraction of occupied volume approaches 0.2. An exponential function can be fitted to the data (dashed line), providing a simple model of saturation; the probability of

excitation is

$$p_e \approx \exp \left( -23.8 \left[ \frac{N_e V_B}{V} \right]^{1.29} \right). \quad (42)$$

When calculating the susceptibility from Eqs. (18) and (37), one has to multiply the oscillator strengths  $F$  by the above probability. This is a similar approach to that one used in [10,13], where also an exponential function  $\exp(-AN_e V_B/V)$  with one fitted constant  $A$  was used.

Finally, to calculate the number of excitons (and thus the blocked volume), one can consider the power to sustain a single exciton

$$P_1 = \frac{E_j}{\tau_j}, \quad (43)$$

where  $E_j$  and  $\tau_j$  are the energy and lifetime of excitonic state. The number of excitons  $N_e$  is

$$N_e = \frac{P_A}{P_1}, \quad (44)$$

where  $P_A$  is the absorbed laser power; for a sufficiently thick sample, it is equal to the total laser power.

As a first verification of the presented theoretical description, one can examine the results obtained in the asymptotic limit of a very large thickness, e.g., a bulk crystal. The results

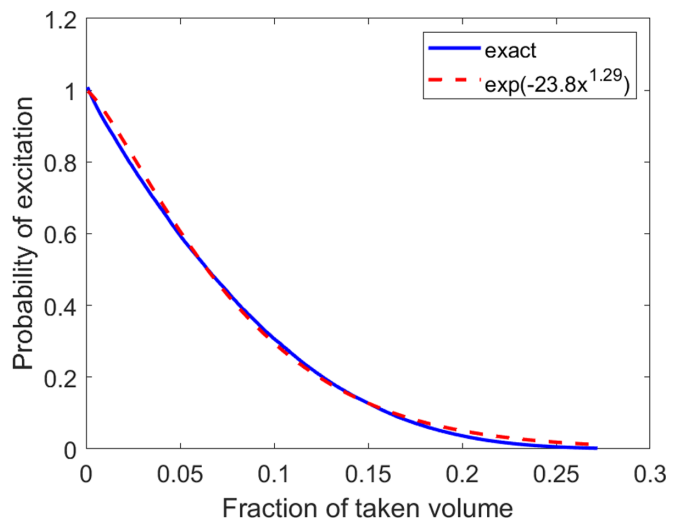


FIG. 2. The probability of excitation as a function of the volume occupied by the Rydberg blockade.

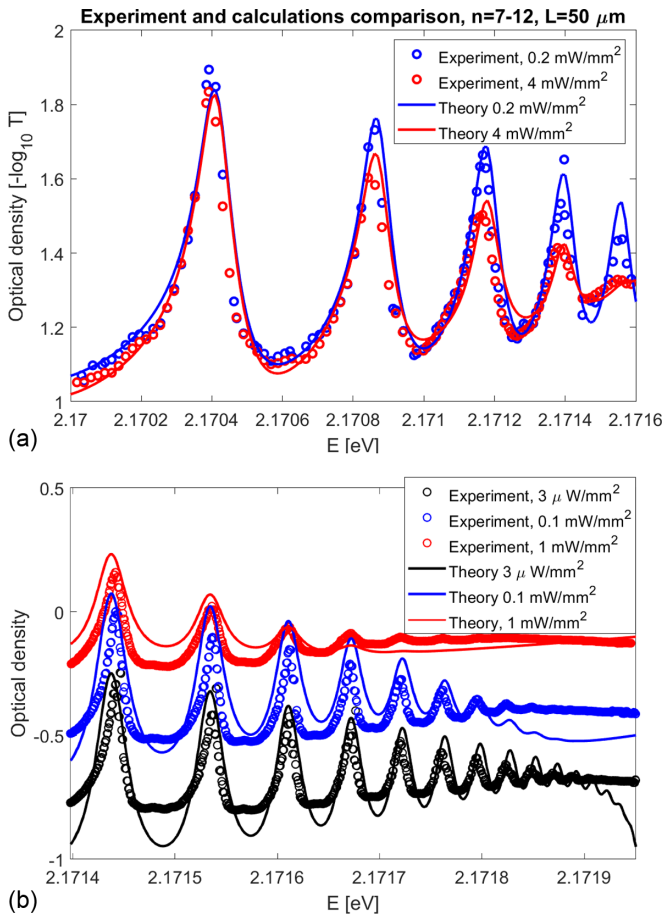


FIG. 3. (a) Calculated optical density, compared to experimental results in bulk crystal [10]. (b) Absorption spectrum compared to the data from [1].

of such a comparison are presented in Fig. 3. Specifically, Fig. 3(a) depicts the calculated optical density spectrum in the region of  $j = 6-11$  excitonic states, for two illumination powers. One can notice a quick decrease of absorption in the high power regime, approximately proportional to blockade volume  $\sim j^7$ . This is the so-called optical bleaching [1]. The same result can be seen in Fig. 3(b), where calculations are compared to the experimental data from [1]. A very good agreement obtained in a wide range of powers and across multiple excitonic states indicates that the saturation model in Eq. (42) is sufficiently precise. However, due to this broad range of states and powers, it is difficult to precisely estimate the model accuracy. For example, the simulation assumes that excitons are static; in reality, their thermal motion can affect their packing (e.g., the fraction of volume taken when saturation occurs). Likewise, the power distribution within the laser beam and its gradual absorption along the propagation distance will have an impact on the blockade effect.

## V. SELF-KERR NONLINEARITY

In the self-Kerr effect the refractive index is changed due to the response of the incoming field itself, in other words it consists of the change of the refractive index of the medium with a variation of the propagating light intensity. The third-order nonlinear susceptibility is the basis of theoretical description

of this phenomenon. The nonlinear optical response is conveniently described in terms of a field-dependent index  $n(E)$  defined as

$$n^2(E) = 1 + \chi = \epsilon_b + \chi^{(1)} + \chi^{(3)}|E|^2 + \dots \quad (45)$$

The real part of the nonlinear susceptibility defines the nonlinear index of refraction, which characterizes the so-called Kerr media,  $n_2 = \frac{Re\chi^{(3)}}{c\epsilon_0 n_0^2}$ , with  $n_0^2 = 1 + \chi^{(1)}$ .

The self-Kerr interaction is an optical nonlinearity that produces a phase shift proportional to the square of the field intensity (or a number of photons in the field). In the Kerr medium the phase of an electromagnetic wave propagating at the distance  $L$  increases and the increment in phase due to an intensity-dependent term is proportional to the distance and to the square of the electric field strength, which is called self-phase modulation. The phase shift is calculated from

$$\Delta\Phi = \frac{\omega L}{c} [n(|E|^2) - n(0)]. \quad (46)$$

The considerable nonlinear susceptibility of the Rydberg excitonic system, further amplified in a thin quantum well, is expected to cause a noticeable phase shift even for small  $L \sim 100$  nm. The confinement states, even when not directly visible, still contribute to the total height of the excitonic line, increasing  $\chi^{(3)}$  and phase shift.

## VI. RESULTS

Due to the limited amount of experimental data regarding nonlinear properties of  $\text{Cu}_2\text{O}$  quantum wells, as a first step we verify our calculations with a comparison to a bulk medium. It should be stressed that while the calculated spectra approach the bulk ones as  $L \rightarrow \infty$ , the presented method is derived under the assumptions of strong confinement and long-wave approximation, so it yields fully correct results only for the well thickness comparable to exciton radius, which for an average value of  $j \sim 3$  implies well thickness significantly below  $1 \mu\text{m}$ . In contrast to [14], where weak confinement regime is studied, the confinement affects the relative motion of the electron-hole pair.

As mentioned above, one can make a rough comparison with experimental results in bulk medium by assuming a large value of  $L$ , skipping the wide quantum well regime at moderate  $L \sim 1 \mu\text{m}$ . The linear and nonlinear parts of susceptibility have been calculated from Eqs. (18) and (37) in a wide range of laser powers and for a thick crystal  $L = 50 \mu\text{m}$ . The results are shown in Fig. 4. The calculated spectra are in the range from  $j = 2$  exciton resonance (2.161 meV) to the band gap (2.172 meV). The effect of the Rydberg blockade is included in calculations by multiplying the obtained susceptibility by the factor  $p_e$  [Eq. (42)]; as the power increases, the density of excitons reaches saturation and  $p_e \rightarrow 0$ . In such a way one is able to control whether one is still in the regime, in which additional effects due to the Rydberg blockade preventing the transmission are absent, and do not influence the excitons-light interaction. One can see that the overall amplitude of the linear susceptibility changes on the order of  $10^{-4}$  and the nonlinear part is approximately 3 orders of magnitude lower. As expected, the number of observed resonances is strongly dependent on the power  $P = \frac{1}{2}cS_b\epsilon|E|^2$ , where  $S_b = 0.1 \text{ mm}^2$  is the beam area; for

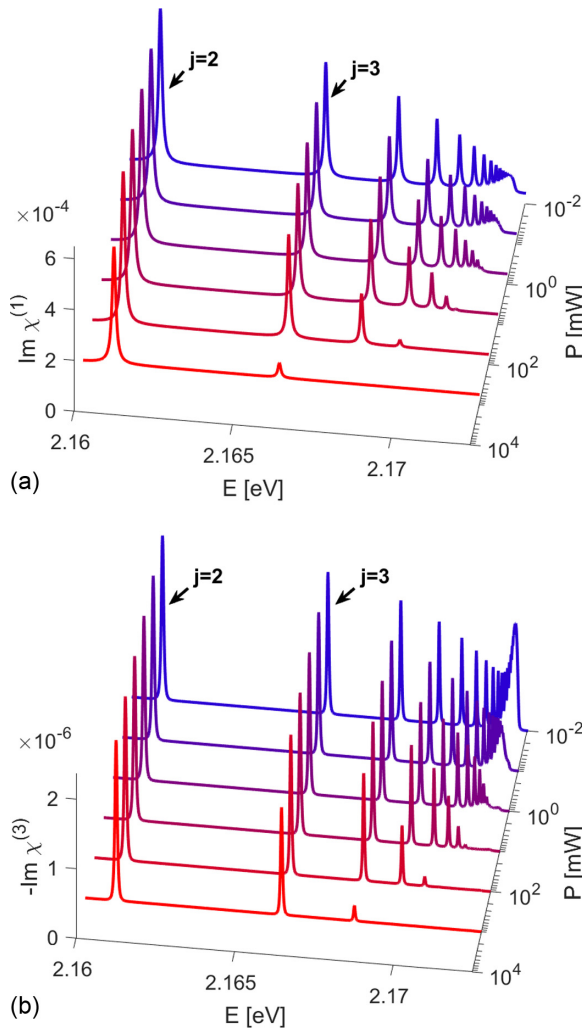


FIG. 4. Imaginary parts of linear  $\chi^{(1)}$  and nonlinear  $\chi^{(3)}$  susceptibility in a bulk crystal ( $L = 50 \mu\text{m}$ ), for selected laser powers.

$P = 1 \text{ W}$ , the bleaching is considerable even for  $j = 3$ . The results are consistent with our previous calculations in a bulk medium [8,10], as well as experimental observations [32] and indicate that the model in Eq. (42) is correct.

As the next step, let us consider a thin  $L = 100 \text{ nm}$  quantum well. In such a system, one can expect that the absorption spectrum will contain multiple confinement states corresponding to the quantum number  $N = 1, 2, 3, \dots$ . One can expect to observe these states for strongly confined excitons, e.g., when the exciton diameter approaches the well thickness. This is the case shown in Fig. 5. Although there is no strict upper limit on the confinement state number  $N_{\text{max}}$ , in practice only a few lowest confinement states are observable and thus in calculations one can assume  $N_{\text{max}} = 10$ . For clarity, the energy range between the third excitonic state ( $j = 2$ ) and the band gap is chosen; lower excitonic states do not meet the criterion for strong confinement and thus no confinement states are visible. The linear part of susceptibility is consistent with the results presented in [15] for the case of a quantum well. Specifically, one can see a series of secondary peaks originating from every excitonic line, which shift towards high energy as  $L$  becomes very small. It should be stressed that these lines corresponding to confinement states are only detectable

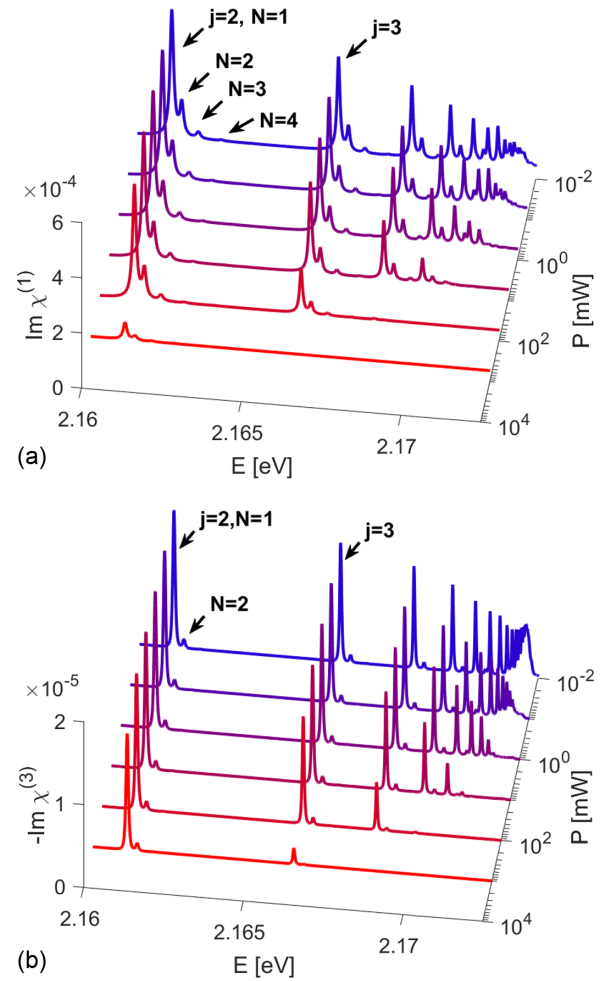


FIG. 5. Imaginary parts of linear  $\chi^{(1)}$  and nonlinear  $\chi^{(3)}$  susceptibility in  $L = 100 \text{ nm}$  quantum well, for selected laser powers.

in the case of a very thin quantum well; in the micrometer-sized nanoparticles, the energy spacing between these lines is small enough that they completely overlap, forming a single, broadened excitonic line [17]. Moreover, in this size range, one cannot observe oscillations of the absorption coefficient caused by the spatial matching between the center-of-mass exciton motion and light waves [18]. Naturally, a very small absorption of a thin sample makes a direct observation of confinement states challenging. Moreover, just like in the case of large quantum dots [17], the oscillator strength of excitonic states decreases faster than  $j^{-3}$ ; this is also consistent with the observations in [14]. This effect, in addition to the broadening and chaotic “background” formed by multiple confinement lines, puts an upper limit on the maximum principal number of the observable state.

The nonlinear susceptibility shown in Fig. 5(b) is apparently similar to the bulk case in Fig. 4. The influence of the confinement on the nonlinear part  $\chi^{(3)}$  is complex. One can see from Eq. (40) that oscillating terms of  $V_{N_e, N_h}$  interplay with slowly varying factors  $\lambda_{\text{th } e, h}$ , describing plasma effects, resulting in an absorption attenuation. Namely, the confinement lines are much less pronounced and only the  $N = 1$  line is readily visible. This effect follows from Eq. (38).



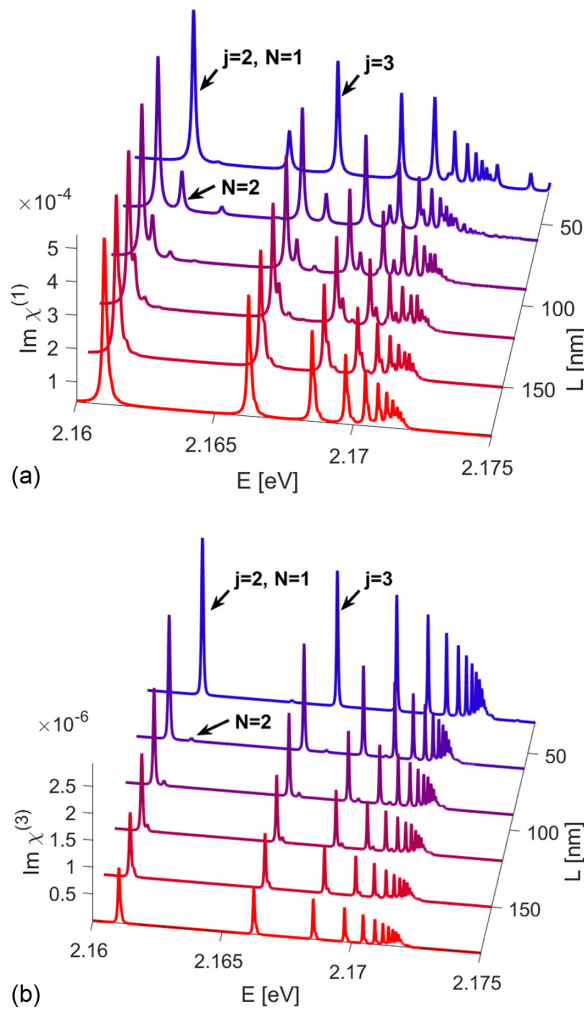


FIG. 6. Imaginary parts of linear  $\chi^{(1)}$  and nonlinear  $\chi^{(3)}$  susceptibility for selected values of quantum well thickness, for  $P = 0.1$  mW.

For low-dimensional systems the nonlinear optical effects depend strongly on the shape of the confinement potentials. For the above-used no-escape boundary conditions we obtained the expressions  $V_{N_e, N_h}$  decaying as  $N^{-1}$ . The physics behind this is that the rapid motion of electrons and holes in the confinement in  $z$  direction, especially for states with higher  $N$ , hinders the creation of plasma which is responsible for the reduction of the absorption while the linear absorption does not depend on  $N$ . For low dimensional systems the nonlinear optical effects depend strongly on the shape of the confinement potentials. In the considered quantum well with no-escape boundary conditions, the overall amplitude of the nonlinear part of the susceptibility is enhanced as compared to bulk system. The influence of the confinement on the nonlinear part of  $\chi^{(3)}$  is more complex. One can see that oscillating functions  $V_{N_e, N_h}$ , characteristic for low dimensional confined systems, interplay with relatively slowly varying exponential functions due to plasmonic terms, which results in increasing of the nonlinear absorption.

Next, Fig. 6 shows the susceptibility spectra calculated for low laser power and various values of thickness. One can see that both confinement lines and the main excitonic

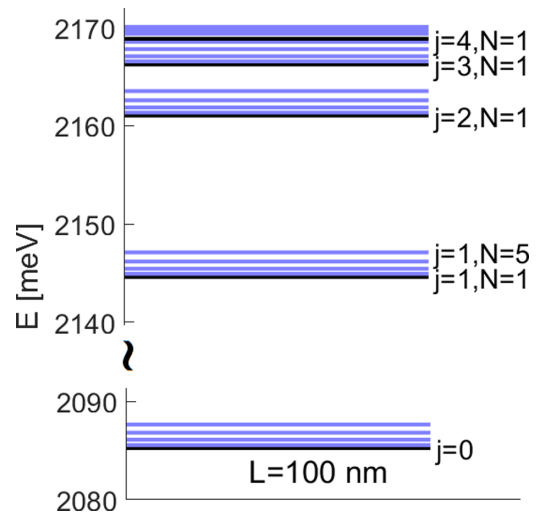


FIG. 7. Schematic representation of excitonic (black) and confinement (blue) energy levels.

lines are blueshifted in the limit of small  $L$ ; as noted in [14], the confined exciton gains additional energy and this energy shift is most pronounced for  $L < 4a_B$ , which is approximately 100 nm for  $n = 10$  excitons. On the other hand, it is known that excitons cannot form in quantum dots when the dot size  $r < 0.4a_B$  [14] which indicates the lower limit of applicability of our theoretical description. As before, the lines corresponding to the confinement states are mostly invisible in the nonlinear susceptibility spectrum. In the linear part, one can see that peaks due to those states, located closely to those due to main excitonic states at  $L = 100$  nm, shift quickly towards higher energy for smaller  $L$  because of the changing proportion between confinement energy and excitonic state energy. Due to this divergence, a considerable mixing of states occurs and also many lines can be visible in the energy region above the band gap. As mentioned before, the nonlinear part of susceptibility is enhanced in a thin quantum well; in Fig. 6(b) one can observe that absorption peaks become higher as  $L$  decreases. The confinement of electrons and holes in a QW results in, illustratively speaking, “squeezing” of excitons, which increases the binding energy and the oscillator strength of excitons, thus leading to an enhancement of the absorption.

Figure 7 shows a schematic representation of energy levels in the above-discussed system (low power,  $L = 100$  nm). For completeness, the energy of the lowest  $1S$  exciton ( $j = 0$ ) is included; however, in this work we only consider  $P$  excitons. One can see that the mixing of states occurs already for  $j = 3$ .

Finally, we can explore the real part of susceptibility and the associated Kerr shift. Naturally, as follows from the Kramers-Kronig relations, each peak in the absorption spectrum corresponds to a region of anomalous dispersion, where  $Re \chi$  and thus also phase shift changes sign. This is visible in Fig. 8(a). As mentioned before, the confinement states are barely visible in the nonlinear part of susceptibility and thus the spectrum is dominated by lines corresponding to excitonic states  $j = 0, 1, 2, \dots$ . Again, we see a divergence towards higher energy as  $L$  decreases and also a reduction of phase shift in the limit of small  $L$  due to the reduced optical length  $nL$  in Eq. (46). Even for a relatively low thickness

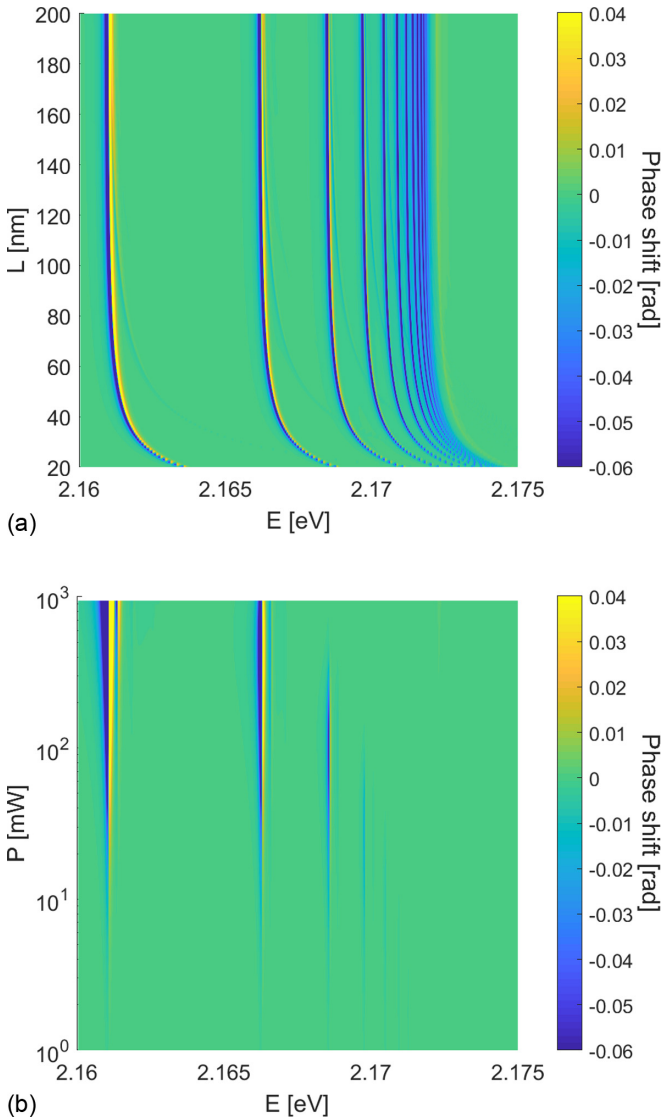


FIG. 8. The self-Kerr shift as a function of (a) quantum well thickness and (b) light power.

$L < 100$  nm, one can observe a phase shift on the order of 50 mrad. The dependence of phase shift on the laser power is shown in Fig. 8(b). Overall, the lower excitonic states provide a larger phase shift due to their larger oscillator strengths. The shift increases with power but is limited by optical bleaching caused by the Rydberg blockade; one can see that the influence of higher states vanishes at high power. On the other hand, in the relatively lower power regime, the stronger nonlinear properties of upper states result in a considerable phase shift. A useful measure of the nonlinearity is the maximum phase shift that can be obtained throughout the whole spectrum. The results calculated for a range of input powers are shown in Fig. 9(a). As expected, the power dependence is linear due to the  $|E|^2 \sim P$  factor in Eq. (46). However, the dependence on thickness, shown in Fig. 9(b), is more complicated. Initially, as  $L$  increases, the phase shift is also rapidly increasing, starting from  $\Delta\Phi(L \rightarrow 0) = 0$ . However, at some point, the increase of the optical length is compensated by the decrease of  $\chi^{(3)}$ , which is enhanced in very

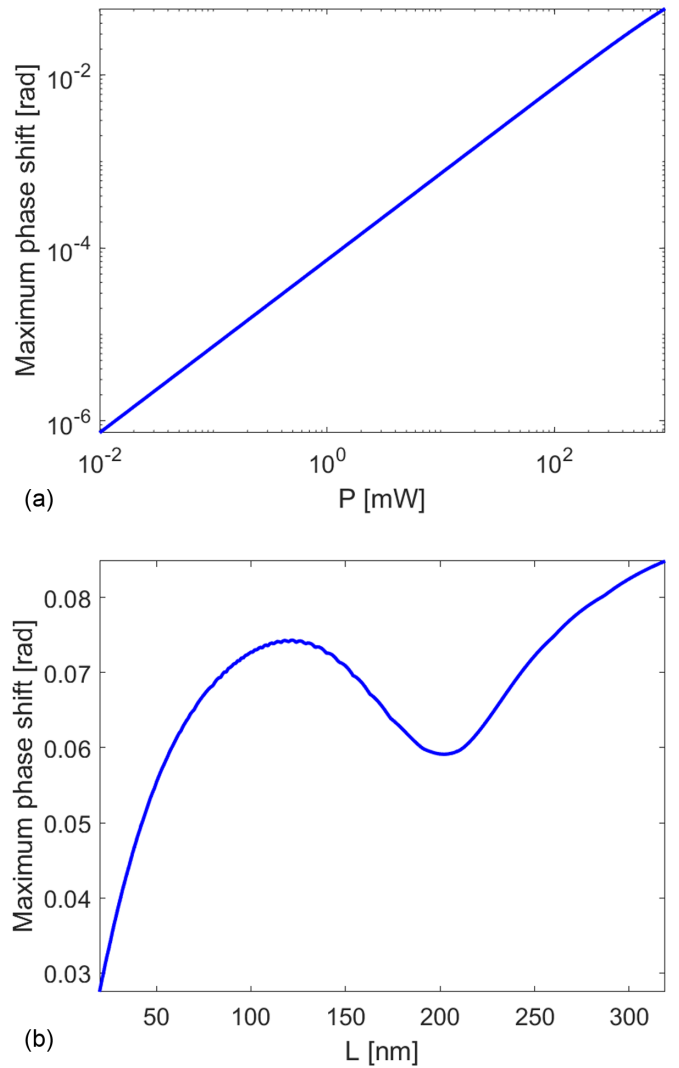


FIG. 9. The maximum value of self-Kerr phase shift as a function of (a) light power and (b) quantum well thickness.

thin wells. Thus, the phase shift reaches a local maximum and then starts decreasing with increasing  $L$ . Eventually, in the region of  $L \sim 300$  nm, the value of  $\chi^{(3)}$  stabilizes on the same level as in bulk medium and the phase shift again becomes linearly dependent on optical length. One can also notice slight oscillations in Fig. 9(b) in the region  $L \sim 100$  nm. In this regime, the confinement states are mostly visible; the thickness-dependent overlapping of multiple states slightly affects the maximum value of the susceptibility, and thus the phase shift. In conclusion, the choice of quantum well thickness, input power, and specific excitonic state to realize a self-Kerr shift is highly nontrivial, with multiple trade-offs influenced by amplification of nonlinear properties, overlap of confinement states, and the Rydberg blockade.

## VII. CONCLUSIONS

In summary, we have studied the nonlinear interaction between an electromagnetic wave and Rydberg excitons in a  $\text{Cu}_2\text{O}$  quantum well using the real density matrix approach, incorporating the control of the Rydberg blockade. Our

theoretical, analytical results for linear and nonlinear absorption are illustrated by numerical calculations and indicate the potential experimental conditions for the best observation of confinement states in linear and nonlinear optical spectra. We show that a clear separation of confinement states and an amplification of nonlinear properties of the system are possible in sufficiently thin ( $L < 100$  nm) quantum wells. The interplay between nonlinearity enhancement and optical length of the system is discussed. We theoretically demonstrate that the Kerr nonlinearity and significant self-phase modulation are accomplished in a semiconductor quantum well with REs.

In short, our work provides insights into the nonlinear interactions of RE with photons in quantum-confined systems, opening interesting opportunities to explore Rydberg excitons for future optoelectronic nanoscale applications. We hope that

our results might be useful for future direct integration of Rydberg confined states with nanophotonic devices.

#### APPENDIX A: COEFFICIENTS A AND B

Denoting by  $\tilde{f}_{0e}$  and  $\tilde{f}_{0h}$  the modified Boltzmann distributions  $f_{0e}$  and  $f_{0h}$  for electron and holes, respectively, projections of  $f_{0e,h}$  on the eigenfunctions  $\Psi_{\ell 1 N_e N_h}$  are given by the following expressions:

$$\langle \Psi_{\ell N_e N_h} | \tilde{f}_{0e}(\mathbf{r}) \rangle = A_{\ell N_e N_h},$$

$$\langle \Psi_{\ell N_e N_h} | \tilde{f}_{0h}(\mathbf{r}) \rangle = B_{\ell N_e N_h},$$

which can be used to calculate the constants

$$\begin{aligned} A_{\ell N_e N_h} &= \langle \psi_j(r, \phi) | \tilde{f}_{0e}^{\parallel}(r, \phi) \rangle \langle \Psi_{N_e N_h} | \tilde{f}_{0e}^{\perp}(z_e, z_h) \rangle \\ &= \sqrt{\frac{\pi}{2}} \frac{1}{\kappa_{\ell}^{1/2}} \mathcal{A} (2\kappa_{\ell})^{\beta} M(-\ell, 3, 4\kappa_{\ell} \rho_0) \sqrt{(\ell+1)(\ell+2)} I_{N_e N_h}^{(e)}, \\ B_{\ell N_e N_h} &= \langle \psi_j(r, \phi) | \tilde{f}_{0h}^{\parallel}(r, \phi) \rangle \langle \Psi_{N_e N_h} | \tilde{f}_{0h}^{\perp}(z_e, z_h) \rangle \\ &= \sqrt{\frac{\pi}{2}} \frac{1}{\kappa_{\ell}^{1/2}} \mathcal{B} (2\kappa_{\ell})^{\gamma} M(-\ell, 3, 4\kappa_{\ell} \rho_0) \sqrt{(\ell+1)(\ell+2)} I_{N_e N_h}^{(h)}, \end{aligned}$$

where the following approximation has been used:

$$\begin{aligned} \langle \psi_j(r, \phi) | \tilde{f}_{0e}^{\parallel}(r, \phi) \rangle &= \int_0^{\infty} \rho d\rho R_{\ell 1}(\rho) \sqrt{\frac{\pi}{2}} \frac{\rho}{\tilde{\lambda}_{\text{the}}} \exp\left[-\frac{\rho^2}{2\tilde{\lambda}_{\text{the}}^2}\right] \\ &= \int_0^{\infty} \rho d\rho \sqrt{\frac{\pi}{2}} \frac{\rho}{\tilde{\lambda}_{\text{the}}} \exp\left[-\frac{\rho^2}{2\tilde{\lambda}_{\text{the}}^2}\right] C_{\ell}(4\kappa_{\ell}\rho) e^{-2\kappa_{\ell}\rho} M(-\ell, 3, 4\kappa_{\ell}\rho) \\ &\approx \frac{4\kappa_{\ell}}{\tilde{\lambda}_{\text{the}}} \sqrt{\frac{\pi}{2}} C_{\ell} M(-\ell, 3, 4\kappa_{\ell}\rho_0) \int_0^{\infty} \rho^3 d\rho e^{-2\kappa_{\ell}\rho - \frac{\rho^2}{2\tilde{\lambda}_{\text{the}}^2}} \\ &= \frac{1}{4\kappa_{\ell}^3 \tilde{\lambda}_{\text{the}}} \sqrt{\frac{\pi}{2}} C_{\ell} M(-\ell, 3, 4\kappa_{\ell}\rho_0) \exp[f(x, z)] \\ &= \frac{1}{2\kappa_{\ell}^{3/2} \tilde{\lambda}_{\text{the}}} \sqrt{\frac{\pi}{2}} \sqrt{(\ell+1)(\ell+2)} M(-\ell, 3, 4\kappa_{\ell}\rho_0) \exp[f(x, z)], \\ f(x, z) &= 4 \ln z_{\ell}^{(e)} + 3 \ln x_{\ell}^{(e)} + \ln[\sigma_{\ell}^{(e)} \sqrt{2\pi}] - \frac{1}{2} x_{\ell}^{(e)2} - z_{\ell}^{(e)} x_{\ell}^{(e)}, \end{aligned}$$

and the integral is evaluated as follows:

$$\begin{aligned} \int_0^{\infty} \rho^3 d\rho e^{-2\kappa_{\ell}\rho - \frac{\rho^2}{2\tilde{\lambda}_{\text{the}}^2}} &= \frac{1}{(2\kappa_{\ell})^4} (z_{\ell}^{(e)})^4 \Gamma(4) e^{(z_{\ell}^{(e)})^2/4} D_{-4}(z_{\ell}^{(e)}), \\ z_{\ell}^{(e)} &= 2\kappa_{\ell} \tilde{\lambda}_{\text{the}} = \frac{2\tilde{\lambda}_{\text{the}}}{2\ell+3}. \end{aligned}$$

The  $D_{-4}[z_{\ell}^{(e)}]$  is the parabolic cylinder function [29] and

$$z_{\ell}^{(e)} = 2\kappa_{\ell} \tilde{\lambda}_{\text{the}} = \frac{2\tilde{\lambda}_{\text{the}}}{2\ell+3}, \quad \tilde{\lambda}_{\text{the}} = \frac{\lambda_{\text{the}}}{a^*}.$$

The term containing function  $D_\nu$  can be approximated as follows:

$$\begin{aligned} z_\ell^{(e)4} \Gamma(4) e^{z_\ell^{(e)2}/4} D_{-4}[z_\ell^{(e)}] &\approx z_\ell^{(e)4} \sigma_\ell^{(e)} \sqrt{2\pi} \exp\{f[x_\ell^{(e)}]\}, \\ x_\ell^{(e)} &= \frac{\sqrt{12 + z_\ell^{(e)2}} - z_\ell^{(e)}}{2}, \\ \sigma_\ell^{(e)} &= \left(1 + \frac{3}{x_\ell^{(e)2}}\right)^{-1/2}, \\ f[x_\ell^{(e)}] &= 3 \ln x_\ell^{(e)} - \frac{1}{2} x_\ell^{(e)2} - z_\ell^{(e)} x_\ell^{(e)}. \end{aligned}$$

### APPENDIX B: CALCULATION OF $\chi^{(3)}$

Equation (37) can be written in the form

$$\chi^{(3)}(\omega) = -\epsilon_0(\epsilon_b \Delta_{LT})^2 a^{*3} e^{-4\rho_0} \left(\frac{1}{\Gamma_{01}}\right) \sum_{j n_e n_h} \Gamma_j \langle \Psi_{N_e N_h} \rangle_L \frac{\Psi_{j n_e n_h}(r_0) \sqrt{f_j}}{(E_{T j n_e n_h} - \hbar\omega)^2 + \Gamma_j^2} \sum_{\ell N_e N_h} \frac{\sqrt{f_\ell} E_{T 1 \ell N_e N_h} (A_{\ell N_e N_h} + B_{\ell N_e N_h})}{E_{T \ell N_e N_h}^2 - (\hbar\omega + i\Gamma_{\ell N_e N_h})^2},$$

where

$$\Psi_{\ell N_e N_h} = \psi_\ell(r, \phi) \psi_{L, N_e}^{(1D)}(z_e) \psi_{L, N_h}^{(1D)}(z_h),$$

$$\begin{aligned} \psi_{\ell m}(r, \phi) &= R_{\ell m} \frac{e^{im\phi}}{\sqrt{2\pi}} = \frac{1}{a^*} \frac{e^{im\phi}}{\sqrt{2\pi}} e^{-2\kappa_{\ell m} r/a^*} \left(4\kappa_{\ell m} \frac{r}{a^*}\right)^m 4\kappa_{\ell m}^{3/2} \frac{1}{(2m)!} \frac{[(\ell + 2m)!]^{1/2}}{[\ell!]^{1/2}} M\left(-\ell, 2|m| + 1, 4\kappa_{\ell m} \frac{r}{a^*}\right) \\ &= \Phi_m(\phi) C_{\ell m} \left(4\kappa_{\ell m} \frac{r}{a^*}\right)^m e^{-2\kappa_{\ell m} r/a^*} M\left(-\ell, 2|m| + 1, 4\kappa_{\ell m} \frac{r}{a^*}\right), \end{aligned}$$

$$\kappa_{\ell m} = \frac{1}{1 + 2(\ell + |m|)},$$

$$C_{\ell m} = \frac{1}{a^*} 4\kappa_{\ell m}^{3/2} \frac{1}{(2m)!} \frac{[(\ell + 2m)!]^{1/2}}{[\ell!]^{1/2}},$$

$$\psi_{L, N_e}^{(1D)}(z_e) = \sqrt{\frac{2}{L}} \cos\left[(2N_e - 1)\pi \frac{z_e}{L}\right],$$

$$\psi_{L, N_h}^{(1D)}(z_h) = \sqrt{\frac{2}{L}} \cos\left[(2N_h - 1)\pi \frac{z_h}{L}\right],$$

$$A_{\ell N_e N_h} = \langle \Psi_{\ell N_e N_h} | \tilde{f}_{0e}(\mathbf{r}) \rangle,$$

$$A_{\ell N_e N_h} = \langle \psi_\ell(r, \phi) | \tilde{f}_{0e}^\parallel(r, \phi) \rangle \langle \Psi_{N_e N_h} | \tilde{f}_{0e}^\perp(z_e, z_h) \rangle,$$

$$B_{\ell N_e N_h} = \langle \psi_\ell(r, \phi) | \tilde{f}_{0h}^\parallel(r, \phi) \rangle \langle \Psi_{N_e N_h} | \tilde{f}_{0h}^\perp(z_e, z_h) \rangle,$$

$$\Psi_{N_e N_h} = \psi_{L, N_e}^{(1D)}(z_e) \psi_{L, N_h}^{(1D)}(z_h),$$

$$\tilde{f}_{0e}(\mathbf{r}) = \tilde{f}_{0e}(\rho, z_e, z_h, \phi) = \sqrt{\frac{\pi}{2}} \frac{r}{\lambda_{\text{the}}} [\Phi_1(\phi) + \Phi_{-1}(\phi)] \exp\left(-\frac{r^2 + (z_e - z_h)^2 m_e k_B T}{2 \hbar^2}\right)$$

$$= \tilde{f}_{0e}^\perp(z_e, z_h) \tilde{f}_{0e}^\parallel(r, \phi),$$

$$\tilde{f}_{0e}^\perp(z_e, z_h) = \exp\left(-\frac{(z_e - z_h)^2 m_e k_B T}{2 \hbar^2}\right),$$

$$\tilde{f}_{0e}^\parallel(r, \phi) = \sqrt{\frac{\pi}{2}} \frac{r}{\lambda_{\text{the}}} \exp\left(-\frac{r^2 m_e k_B T}{2 \hbar^2}\right) [\Phi_1(\phi) + \Phi_{-1}(\phi)],$$

$$r = \sqrt{x^2 + y^2},$$

(B1)



and

$$\Phi_m(\phi) = \frac{e^{im\phi}}{\sqrt{2\pi}},$$

$$\lambda_{\text{th } e} = \left( \frac{\hbar^2}{m_e k_B \mathcal{T}} \right)^{1/2} = \sqrt{\frac{2\mu}{m_e}} \sqrt{\frac{R^*}{k_B \mathcal{T}}} a^*$$

is the so-called thermal length (here for electrons).

Similarly, for the hole equilibrium distribution, we have

$$\begin{aligned} \tilde{f}_{0h}(\mathbf{r}) &= \tilde{f}_{0h}(\rho, z_e, z_h, \phi) \\ &= \sqrt{\frac{\pi}{2}} \frac{r}{\lambda_{\text{th } h}} [\Phi_1(\phi) + \Phi_{-1}(\phi)] \\ &\quad \times \exp\left(-\frac{r^2 + (z_e - z_h)^2 m_h k_B \mathcal{T}}{2 \hbar^2}\right) \\ &= \tilde{f}_{0h}^\perp(z_e, z_h) \tilde{f}_{0h}^\parallel(r, \phi), \\ \tilde{f}_{0h}^\perp(z_e, z_h) &= \exp\left(-\frac{(z_e - z_h)^2 m_h k_B \mathcal{T}}{2 \hbar^2}\right), \\ \tilde{f}_{0h}^\parallel(r, \phi) &= \sqrt{\frac{\pi}{2}} \frac{r}{\lambda_{\text{th } h}} \exp\left(-\frac{r^2 m_h k_B \mathcal{T}}{2 \hbar^2}\right) \\ &\quad \times [\Phi_1(\phi) + \Phi_{-1}(\phi)], \end{aligned} \quad (\text{B2})$$

TABLE I. Band parameter values for Cu<sub>2</sub>O, masses in free electron mass  $m_0$ .

Parameter	Value	Unit	Reference
$E_g$	2172.08	meV	[1]
$R^*$	87.78	meV	[33]
$\Delta_{LT}$	$1.25 \times 10^{-3}$	meV	[34]
$m_e$	0.99	$m_0$	[35]
$m_h$	0.58	$m_0$	[35]
$\mu$	0.363	$m_0$	
$\mu'$	-2.33	$m_0$	
$M_{\text{tot}}$	1.56	$m_0$	
$a^*$	1.1	nm	[33]
$r_0$	0.22	nm	[28]
$\epsilon_b$	7.5		[1]
$T_1$	500	ns	

with the hole thermal length

$$\lambda_{\text{th } h} = \left( \frac{\hbar^2}{m_h k_B \mathcal{T}} \right)^{1/2} = \sqrt{\frac{2\mu}{m_h}} \sqrt{\frac{R^*}{k_B \mathcal{T}}} a^*,$$

with the radial part  $\psi_j(r, \phi) |f_{0e}^\parallel(r, \phi)\rangle$  defined in Appendix A.

### APPENDIX C: TABLE OF PARAMETERS

All the relevant parameters used in calculations, along with their literature sources, are summarized in Table I

- [1] T. Kazimierczuk, D. Fröhlich, S. Scheel, H. Stolz, and M. Bayer, *Nature (London)* **514**, 343 (2014).
- [2] J. Heckötter, M. Freitag, D. Fröhlich, M. Aßmann, M. Bayer, M. A. Semina, and M. M. Glazov, *Phys. Rev. B* **95**, 035210 (2017).
- [3] M. Aßmann and M. Bayer, *Adv. Quantum Technol.* **3**, 1900134 (2020).
- [4] S. A. Lynch, C. Hodges, S. Mandal, W. Langbein, R. P. Singh, L. A. P. Gallagher, J. D. Pritchett, D. Pizzey, J. P. Rogers, C. S. Adams, and M. P. A. Jones, *Phys. Rev. Mater.* **5**, 084602 (2021).
- [5] J. Heckötter, V. Walther, S. Scheel, M. Bayer, T. Pohl, and M. Assmann, *Nat. Commun.* **12**, 3556 (2021).
- [6] L. A. P. Gallagher, J. P. Rogers, J. D. Pritchett, R. A. Mistry, D. Pizzey, Ch. S. Adams, M. P. A. Jones, P. Grünwald, V. Walther, Ch. Hodges, W. Langbein, and S. A. Lynch, *Phys. Rev. Res.* **4**, 013031 (2022).
- [7] K. Orfanakis, S. Rajendran, V. Walther, T. Volz, T. Pohl, and H. Ohadi, *Nat. Mater.* **21**, 767 (2022).
- [8] S. Zielińska-Raczyńska, G. Czajkowski, K. Karpiński, and D. Ziemkiewicz, *Phys. Rev. B* **99**, 245206 (2019).
- [9] V. Walther, P. Grünwald, and T. Pohl, *Phys. Rev. Lett.* **125**, 173601 (2020).
- [10] C. Morin, J. Tignon, J. Mangeney, S. Dhillon, G. Czajkowski, K. Karpiński, S. Zielińska-Raczyńska, D. Ziemkiewicz, and T. Boulier, [arXiv:2202.09239](https://arxiv.org/abs/2202.09239) [Phys. Rev. Lett. (to be published)].
- [11] V. Walther, R. Johné, and T. Pohl, *Nat. Commun.* **9**, 1309 (2018).
- [12] D. Ziemkiewicz and S. Zielińska-Raczyńska, *Opt. Lett.* **43**, 3742 (2018).
- [13] D. Ziemkiewicz and S. Zielińska-Raczyńska, *Opt. Express* **27**, 16983 (2019).
- [14] A. Konzelmann, B. Frank, and H. Giessen, *J. Phys. B: At. Mol. Opt. Phys.* **53**, 024001 (2020).
- [15] D. Ziemkiewicz, K. Karpiński, G. Czajkowski, and S. Zielińska-Raczyńska, *Phys. Rev. B* **101**, 205202 (2020).
- [16] D. Ziemkiewicz, G. Czajkowski, K. Karpiński, and S. Zielińska-Raczyńska, *Phys. Rev. B* **103**, 035305 (2021).
- [17] K. Orfanakis, S. K. Rajendran, H. Ohadi, S. Zielińska-Raczyńska, G. Czajkowski, K. Karpiński, and D. Ziemkiewicz, *Phys. Rev. B* **103**, 245426 (2021).
- [18] M. Takahata, K. Tanaka, and N. Naka, *Phys. Rev. B* **97**, 205305 (2018).
- [19] S. Steinhauer, M. A. M. Versteegh, S. Gyger, A. Elshaari, B. Kunert, A. Mysyrowicz, and V. Zwiller, *Commun. Mater.* **1**, 11 (2020).
- [20] H. R. Hamed and M. R. Mehmannaavaz, *Phys. E* **66**, 309-316 (2015).
- [21] S. G. Kosionis, A. F. Terzis, and E. Paspalakis, *J. Appl. Phys.* **109**, 084312 (2011).
- [22] C. Zhu and G. Huang, *Opt. Express* **19**, 23364 (2011).
- [23] H. Qian, Y. Xiao, and Z. Liu, *Nat. Commun.* **7**, 13153 (2016).
- [24] A. Stahl and I. Balslev, *Electrodynamics of the Semiconductor Band Edge* (Springer, Berlin, 1987).

- [25] G. Czajkowski, F. Bassani, and A. Tredicucci, Polaronic effects in superlattices, *Phys. Rev. B* **54**, 2035 (1996).
- [26] S. Zielińska-Raczyńska, G. Czajkowski, and D. Ziemkiewicz, *Phys. Rev. B* **95**, 075204 (2017).
- [27] D. Ziemkiewicz, G. Czajkowski, K. Karpiński, and S. Zielińska-Raczyńska, *Phys. Rev. B* **104**, 075303 (2021).
- [28] S. Zielińska-Raczyńska, G. Czajkowski, and D. Ziemkiewicz, *Phys. Rev. B* **93**, 075206 (2016).
- [29] M. Abramowitz and I. Stegun, *Handbook of Mathematical Functions* (Dover, New York, 1965).
- [30] D. D. Kang, A. Gross, H. B. Yang, Y. Morita, K. S. Choi, K. Yoshioka, and N. Y. Kim, *Phys. Rev. B* **103**, 205203 (2021).
- [31] D. Frank and A. Stahl, *Solid State Commun.* **52**, 861 (1984).
- [32] J. Heckötter, M. Freitag, D. Fröhlich, M. Assmann, M. Bayer, P. Grünwald, F. Schöne, D. Semkat, H. Stolz, and S. Scheel, *Phys. Rev. Lett.* **121**, 097401 (2018).
- [33] S. Zielińska-Raczyńska, D. Ziemkiewicz, and G. Czajkowski, *Phys. Rev. B* **97**, 165205 (2018).
- [34] H. Stolz, F. Schöne, and D. Semkat, *New J. Phys.* **20**, 023019 (2018).
- [35] N. Naka, I. Akimoto, M. Shirai, and K.-i. Kan'no, *Phys. Rev. B* **85**, 035209 (2012).